Estimation of Spatial Correlation of Drop Size Distribution Parameters and Rain Rate Using NASA's S-Band Polarimetric Radar and 2D Video Disdrometer Network: Two Case Studies from MC3E

V. N. BRINGI, L. TOLSTOY, AND M. THURAI

Department of Electrical and Computer Engineering, Colorado State University, Fort Collins, Colorado

W. A. PETERSEN

Wallops Flight Facility, NASA Goddard Space Flight Center, Wallops Island, Virginia

(Manuscript received 15 October 2014, in final form 16 January 2015)

ABSTRACT

Polarimetric radar data obtained at high spatial and temporal resolutions offer a distinct advantage in estimating the spatial correlation function of drop size distribution (DSD) parameters and rain rate compared with a fixed gauge–disdrometer network. On two days during the 2011 Midlatitude Continental Convective Clouds Experiment (MC3E) campaign in Oklahoma, NASA's S-band polarimetric radar (NPOL) performed repeated PPI scans every 40 s over six 2D video disdrometer (2DVD) sites, located 20–30 km from the radar. The two cases were 1) a rapidly evolving multicell rain event (with large drops) and 2) a long-duration stratiform rain event. From the time series at each polar pixel, the Pearson correlation coefficient is computed as a function of distance along each radial in the PPI scan. Azimuthal dependence is found, especially for the highly convective event. A pseudo-1D spatial correlation is computed that is fitted to a modified-exponential function with two parameters (decorrelation distance R_0 and shape F). The first event showed significantly higher spatial variability in rain rate (shorter decorrelation distance R_0 = 3.4 km) compared with the second event with R_0 = 10.2 km. Further, for the second event, the spatial correlation of the DSD parameters and rain rate from radar showed good agreement with 2DVD-based spatial correlations over distances ranging from 1.5 to 7 km. The NPOL also performed repeated RHI scans every 40 s along one azimuth centered over the 2DVD network. Vertical correlations of the DSD parameters as well as the rainwater content were determined below the melting level, with the first event showing more variability compared with the second event.

1. Introduction

The structure of the rain-rate field has been studied extensively by hydrologists at various spatial and temporal scales, primarily relying on rain gauge networks of various densities. While gauges generally give accurate point measurements, except for a few dense networks (e.g., Huff 1970; Moore et al. 2000; Ciach and Krajewski 2006, hereafter CK06), the areal density is generally not sufficient to accurately characterize the rather extreme spatial variability of rainfall, especially considering convective rain cells with a horizontal extent less than a few kilometers. Further, to capture the statistics of the spatial variations, a large database is necessary, ranging from many months to several years, because of inherent low frequency of rain occurrence over fixed gauge networks. CK06 discuss a number of important aspects of the small-scale spatial correlation function, including dependence on time averaging and the large storm-to-storm variability of the decorrelation distance (1/e-folding distance) and shape factor. They also point to the difficulties in determining the anisotropy of the correlation function using a gauge network.

More recently, disdrometer networks (Tapiador et al. 2010; Jaffrain and Berne 2012) have been used to study the small-scale spatial variability of drop size distribution (DSD) parameters, and this transition from gauges to more modern optical disdrometers (Schönhuber et al. 2008; Löffler-Mang and Joss 2000) can be considered a major step since the rain rate is fundamentally close to the 3.67th moment of the DSD, which itself may be

Corresponding author address: Prof. V. N. Bringi, Department of Electrical and Computer Engineering, Colorado State University, Campus Mail 1373, Fort Collins, CO 80523-1373.
E-mail: bringi@engr.colostate.edu

DOI: 10.1175/JHM-D-14-0204.1

© 2015 American Meteorological Society

considered as a double random variable, that is, the product of the Poisson-distributed number concentration and the (typically) gamma-distributed drop diameter. The most dense optical disdrometer network appears to be that described in Jaffrain and Berne (2012), with 16 units in a $1 \times 1\,\mathrm{km}^2$ area. They compared their spatial correlation data of rainfall at 1- and 15-min temporal resolutions (up to separation of 700 m) with past work by Tokay and Bashor (2010), CK06, and Villarini et al. (2008), but the comparisons (even using a large database in each case) were less than satisfactory, which the authors attribute to the use of different instruments and accuracies, network configuration, size of dataset, and different rain climatologies.

There are only a few past studies on the use of disdrometers to estimate the spatial variability of the DSD (Lee et al. 2009; Tokay and Bashor 2010), but these were limited in the number and type of disdrometers used (3–4) and their spatial configuration. The spatial variability of DSD parameters such as total number concentration (or the normalized intercept parameter N_W; Illingworth and Blackman 2002) and the mass-weighted mean diameter D_m (or, equivalently, the median volume diameter D_0) become relevant for remote sensors such as dual-polarimetric or dual-wavelength radars (either ground-based or satelliteborne systems; Chandrasekar et al. 2008; Hou et al. 2014) that explicitly retrieve these quantities over pixels from 2×2 to $5 \times 5\,\mathrm{km}^2$. Thus, the small-scale or subpixel variability at temporal scales of approximately a few minutes becomes important in several applications, for example, quantitative assessment of the retrieval accuracy (e.g., error–variance separation) in estimating non-uniform beam filling (NUBF) correction factors or in simulation of DSD fields (e.g., Habib and Krajewski 2002; Kozu and Iguchi 1999; Schleiss and Berne 2012). The vertical correlation of DSD parameters has been less well studied but is potentially important for satellite-based dual-wavelength radar retrievals. Given the intrinsic frequencies and viewing angles of satellite-based radars combined with interactions of the beam with the intervening column of hydrometeors and the earth's surface, satellite radar retrieval algorithms are naturally sensitive to the behavior of the column DSD. Vertical correlation properties may potentially serve as a possible added constraint for the retrievals, and when combined with similar information on the horizontal DSD variability, they may be useful for the correction-related NUBF correction factors in tilted rain cells (e.g., for understanding frequency-dependent impacts of three-dimensional NUBF correction factors on path-integrated attenuation correction algorithms and attendant DSD and rain-rate estimation; Short and Iguchi 2011; Meneghini et al. 2013) in deep convection or in quantifying the contribution of vertical variability and the hydrometeor profile characteristics to radar estimation of rain rate at the surface (Habib and Krajewski 2002).

The use of dual-polarimetric radar to study the spatial variability of rainfall was pioneered by Moreau et al. (2009), who used an X-band radar in close proximity (from 5 to 25 km) to a dense network of gauges. The radar was continuously operated in sector plan position indicator (PPI) mode over the gauge network at fixed elevation angle with revisit time of 30 s. While their focus was on the rain-rate field (pixels of $1 \times 1\,\mathrm{km}^2$ and 6-min integration) and not on the DSD parameters, they were able to show excellent comparison between the spatial correlation derived from radar and those from the gauge network over separation distances from 1 to 10 km. They also comment that, within the framework of their experiment, estimating the spatial correlation from the gauge network required about 1 year of data, whereas from radar only a few rain events were required by virtue of a much larger coverage area with a high density of pixels.

More recently, Thurai et al. (2012) used the dual-polarimetric C-band Advanced Radar for Meteorological and Operational Research (ARMOR) over a very narrow sector (5°) with revisit time of ~10 s, essentially dwelling the beam over two collocated 2D video disdrometers (2DVDs) at a short range of 15 km. Using such data from a single, long-duration (4 h) rain event, they were able to derive the spatial correlation function of the two DSD parameters (N_W and D_0) and rain rate R along the beam (relative to the 2DVD location, distance from 0 to 4 km with 250-m resolution). While rather "stable" and "reasonable" correlation versus distance functions were obtained, they could not be independently validated but were shown to be in very good agreement (decorrelation distance and shape parameter) for R with Moreau et al. (2009).

In this paper, NASA's S-band polarimetric radar (NPOL) is used with a 150-m range resolution and with a revisit time of 40 s over an 80° sector within which a network of six 2DVD units was located at short ranges of 20–30 km from the radar. The main goal is to build on the prior work of Thurai et al. (2012) to derive the spatial correlation function of DSD parameters (N_W and D_0) and R as retrieved from polarimetric measurements (radar reflectivity for horizontal polarization Z_h, differential reflectivity Z_{dr}, and specific differential propagation phase K_{dp}) as a function of azimuth from sector PPI data (horizontal correlations) and vertical correlations using RHI scans (with revisit time of 40 s) along the radial to the center of the 2DVD network.

TABLE 1. NPOL specifications.

Frequency	2.7–2.9 GHz
Polarization	H, V: simultaneous transmit and receive
Receiver	RVP900
Variables	Z, Z_{dr}, Φ_{dp}, K_{dp} [also linear depolarization ratio (LDR)*]
Pulse width	0.8–2 μs
PRF	250–2000 Hz
Duty cycle	0.0012 s
Antenna	8.5 m, prime parabolic, no radome
Gain	>44.5 dB
Pointing accuracy	0.1°
Beamwidth	0.9°
Rotation rate	18° s^{-1} max

* In special LDR mode.

2. Instrumentation and data collection

The data used in this study were acquired during the Midlatitude Continental Convective Clouds Experiment (MC3E; see Petersen and Jensen 2012), which was conducted in central Oklahoma in April and May 2011. On several limited occasions during this campaign, NASA's S-band polarimetric radar performed repeated PPI and RHI scans over six 2DVD sites, located 20–30 km from the radar. The scans were repeated approximately every 40 s (revisit time). Such scans were limited during the campaign as NPOL was used to support aircraft flights as well as to capture the entire vertical extent of the deep convective storms with revisit times of 5–10 min.

NPOL is a research-grade dual-polarized S-band system. The nominal radar system parameters are shown in Table 1. The gate spacing is 0.15 km, with typically 1000 gates per beam.

We consider here two cases, one a rapidly evolving multicell rain event (with large drops) that occurred on 24 April and the second a more uniform and widespread rain event that occurred on 11 May 2011. We utilize the repeated PPI and RHI scans to determine the horizontal H and vertical V spatial correlation functions, respectively, for the main DSD parameters, namely, the median volume diameter and the normalized "intercept" parameter, as well as rain rate for the horizontal spatial correlation and liquid (rain) water content (LWC) for vertical correlation.

Figure 1a shows the map of the campaign location within the U.S. Department of Energy's Southern Great Plains (SGP) facility in central Oklahoma. The white triangle depicts the area within which six 2DVDs (low-profile third-generation design; Schönhuber et al. 2008) were sited and the area where the PPI scans were performed, that is, over the azimuth range of 245°–325°, at an elevation angle 0.98°. The RHI scans were performed at an azimuth of 283.5°, over one of the 2DVD sites, with elevation angles ranging from 0° to 18°. Figures 1b and 1c show magnified views of the six 2DVD locations (black crosses) overlaid onto PPI scans from the 24 April and the 11 May 2011 events. The 24 April event (event 1) was an intense multicell complex that mostly evolved within the scan area with very little advection, whereas the 11 May event (event 2) was much more uniform with a long period of trailing stratiform rain over the scan area after initial passage of squall-line-type leading convective cells.

The spacing of the six instruments enables us to determine the "point" spatial correlation functions of the DSD parameters and R calculated from the 2DVD measurements, which in turn can be compared with radar-based estimation of the pixel-based correlation function (this could only be done reliably for the long-duration event 2; event 1 was not long enough for reliable estimation). From meteorological context of the two events and from Figs. 1b and 1c, we expect that the spatial variability will be much higher for event 1 compared to event 2. Figures 2b and 2d show vertical profiles of reflectivity Z from an S-band profiler located at the main SGP facility next to one of the 2DVD units (Figs. 2a,c show the 1-min rain rates from this 2DVD unit at ground level). The time–height profiles for the two events are marked to illustrate the periods during which NPOL PPI and RHI scans with revisit time of 40 s were available. Clearly, event 1 is highly convective with substantial variability in the vertical, whereas event 2 is more uniform (with some evidence of weak embedded convection) with a bright band at 3 km AGL. The rain-rate time series (Figs. 2a,c) from the 2DVD unit next to the S-band profiler shows more variable values for event 1 reaching 40 mm h^{-1} (the other units recorded higher rain rates up to 100 mm h^{-1}), whereas for event 2 the rain rates are more uniform with maximum values <10 mm h^{-1}.

3. Radar data processing

a. Initial steps

The radar data processing consists of several steps, most of which have been described previously [see Bringi et al. (2013a) for NPOL data processing during MC3E and determination of calibration offsets for Z_h and Z_{dr}]. The separation of meteorological echoes from non-meteorological echoes was based on calculation of the standard deviation of differential propagation phase Φ_{dp} over a 10-gate moving window, with a threshold of 10° (Bringi et al. 2006). Even though the attenuation is generally negligible at S band, the reflectivity was corrected using the linear Φ_{dp} method described by Ryzhkov et al. (2005):

$$\Delta Z_h = 0.02\Delta\Phi_{dp}. \quad (1)$$

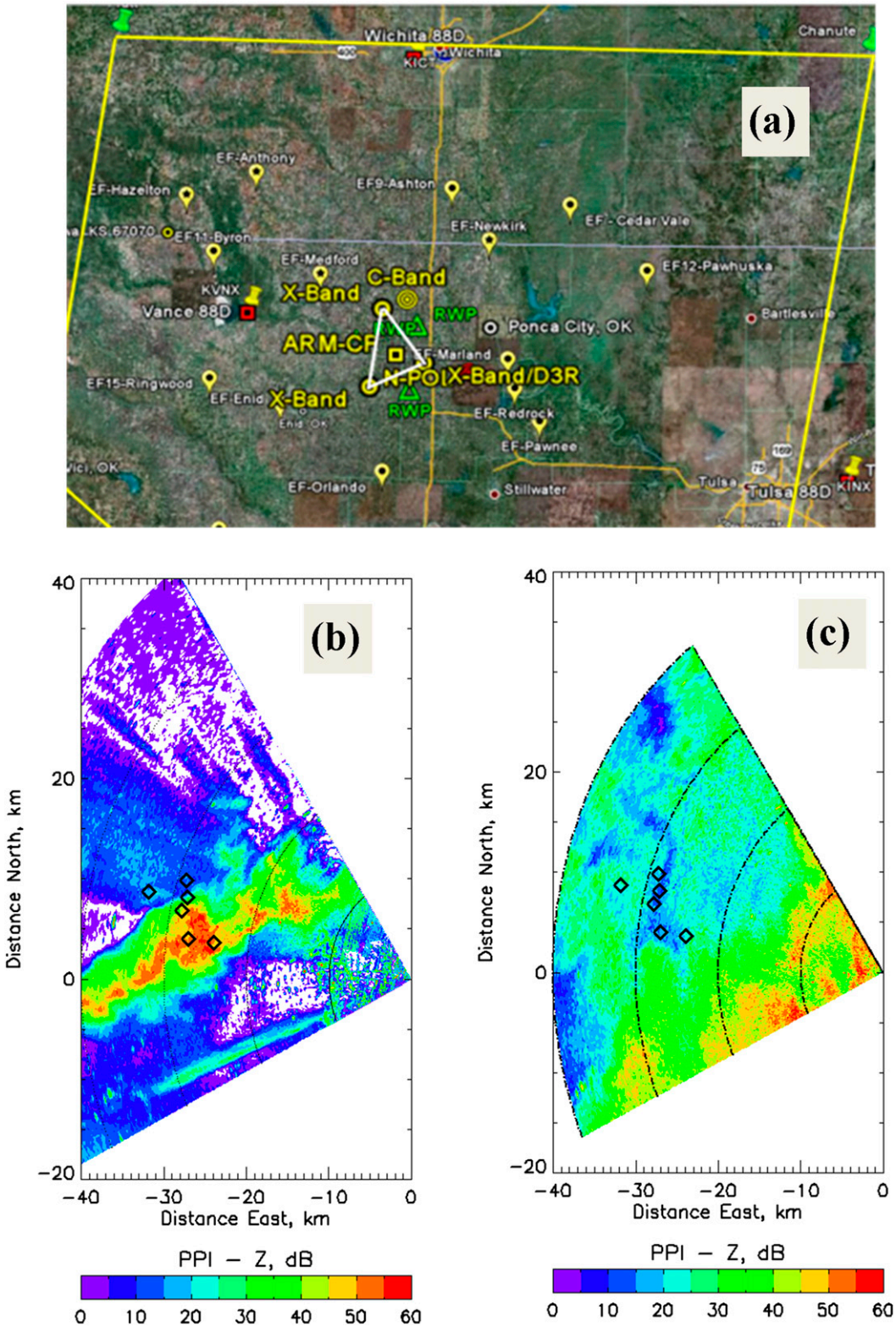

FIG. 1. (a) Map of MC3E study domain, (b) an NPOL PPI scan taken on 24 Apr, and (c) an NPOL PPI scan taken on 11 May 2011. The white triangle in (a) shows the area scanned by radar and within which the six 2DVDs are sited [marked as black diamonds in (b) and (c)].

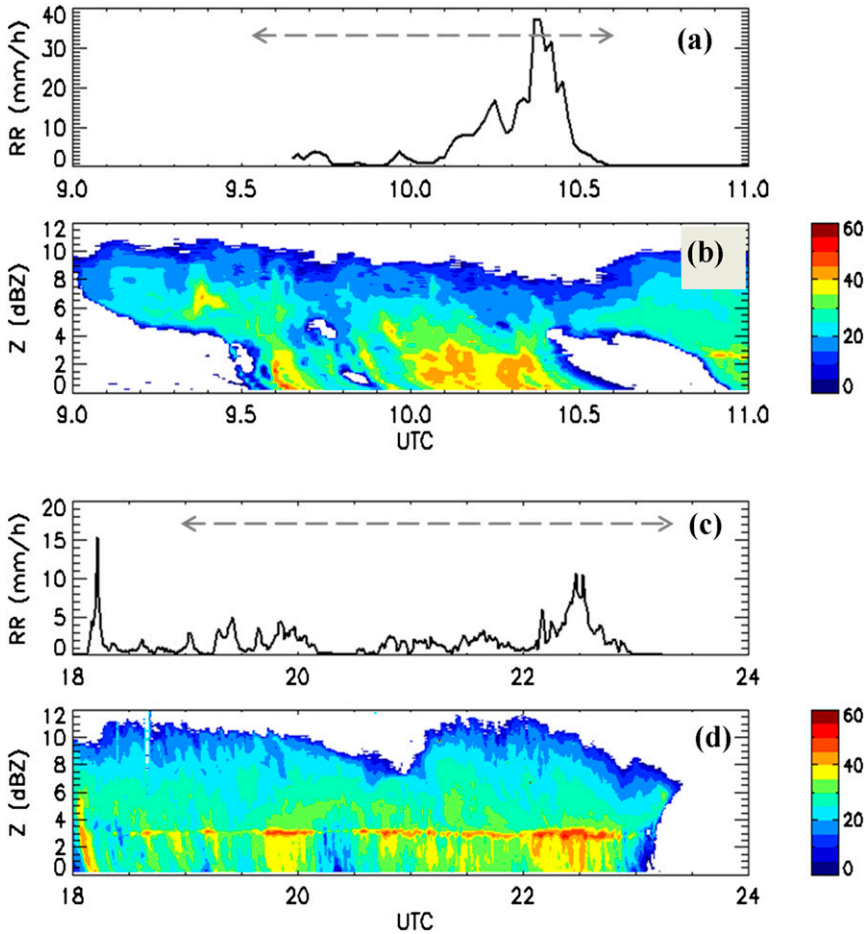

FIG. 2. (a) Rain-rate time series measured by one 2DVD unit at the SGP facility and (b) the reflectivity height profile time series from the S-band profiler (also at the SGP facility) for the 24 Apr event. (c),(d) As in (a),(b), but for the 11 May event. The gray dashed lines in (a),(c) represent the time periods over which the NPOL repeated scans were made.

The coefficient of 0.02 is in units of decibels per degree and is applicable for summertime convection in Oklahoma. Note that the correction is $Z_h(\text{corr}) = Z_h(\text{meas}) + \Delta Z_h$, with $\Delta\Phi_{dp}$ being the path-integrated differential propagation phase from the radar to the range gate of interest.

Similarly, differential reflectivity is corrected for differential attenuation as follows:

$$\Delta Z_{dr} = 0.0042\Delta\Phi_{dp}, \tag{2}$$

where the coefficient 0.0042 is in units of decibels per degree (Ryzhkov et al. 2005). Again, $Z_{dr}(\text{corr}) = Z_{dr}(\text{meas}) + \Delta Z_{dr}$. The K_{dp} parameter was obtained using an iteratively filtered Φ_{dp} methodology as described in Hubbert and Bringi (1995) and using an ad hoc "telescoping" method where a variable number of gates is used, depending on the Z_h value (Bringi et al. 2011), which approximately corresponds to the "light" (9 gates) and "heavy" (25 gates) filtering for computing K_{dp} by Ryzhkov et al. (2005). Prior to calculation of rain rate, D_0, and $\log_{10}(N_W)$, the hail regions of the precipitation were filtered out, using hail detection ratio (HDR; Aydin et al. 1986) with the threshold set at 5 dB (e.g., Brandes et al. 1993; Depue at al 2007).

The 1-min drop size distributions (total of 836) measured by the 2DVD data from six units on 24 April were used (see Bringi et al. 2003) to derive the retrieval algorithms for D_0, N_W, R, and LWC. The drop shapes from the 80-m fall bridge experiment from Thurai et al. (2007) and the canting angle distribution from Huang et al. (2008) were used as input to the scattering calculations. The simulations resulted in the following equations.

1) The median volume diameter (mm) is calculated using the calibrated Z_{dr} data using

$$D_0 = 0.0536Z_{dr}^3 - 0.1971Z_{dr}^2 + 0.6261Z_{dr} + 1.0815; \quad Z_{dr} \geq 1\,\text{dB} \tag{3a}$$

and

$$D_0 = 0.0424Z_{dr}^4 - 0.4571Z_{dr}^3 + 0.6215Z_{dr}^2 + 0.457Z_{dr} + 0.8808; \quad -0.5 < Z_{dr} < 1\,\text{dB}. \tag{3b}$$

2) The intercept parameter of the normalized gamma drop size distribution N_W ($\text{mm}^{-1}\,\text{m}^{-3}$) is estimated from

$$N_W = 19.76\frac{Z_{h_{\text{linear}}}}{D_0^{7.46}}, \tag{4}$$

where $Z_{h_{\text{linear}}}$ is Z_h in linear units. Note that $\log_{10}(N_W)$ is retrieved and used henceforth, but for ease of notation, we still refer to it as N_W unless explicitly stated.

3) The LWC ($\text{g}\,\text{m}^{-3}$) is calculated using

$$\text{LWC} = 3.4566 \times 10^{-4}\frac{Z_{h_{\text{linear}}}}{D_0^{3.46}}. \tag{5}$$

4) The rain rate is calculated using the composite algorithm (see Ryzhkov et al. 2005) using as input (Z_h, Z_{dr}, and K_{dp}):

$$R(Z_h) = 0.0229(Z_{h_{\text{linear}}}^{0.6425}), \tag{6}$$

$$R(K_{dp}) = 34.3(K_{dp}^{0.757}), \tag{7}$$

and

$$R(Z_h, Z_{dr}) = 0.0142\frac{(Z_{h_{\text{linear}}}^{0.77})}{(Z_{dr_{\text{linear}}}^{1.67})}. \tag{8}$$

The above mean fits reduce the retrieval algorithm (or parameterization) error due to DSD variability, which is an important component of the total error for D_0 but less so for N_W and R, where radar measurement errors also play an important role (Thurai et al. 2012; Bringi et al. 2009). Typical fractional standard errors (including both parameterization and radar measurement errors) are estimated to be around 10%, 6%, and 17% for D_0, $\log_{10}(N_W)$, and R, respectively. The block diagram illustrating the composite algorithm and thresholds for step 4 is given in Fig. 6 of Bringi et al. (2013a). The retrieval algorithms in Eqs. (3)–(8) are based on 2DVD-measured DSDs, which are less accurate at the small drop end ($D <$ 0.7 mm or so) because of sensitivity and mismatch problems and at the large drop end ($D >$ 6 mm or so) because of inadequate sampling. Thus, the retrieval of D_0 in Eq. (3) can show systematic error for small D_0 (such as in drizzle) or very large D_0 (such as due to drop sorting in convection). In the events analyzed herein, the disdrometer-derived D_0 values were nearly always in the range $0.5 < D_0 < 2.5$ mm. The accurate retrieval of N_W in light rain is further complicated by the large exponent of D_0 occurring in the denominator of Eq. (4) (i.e., propagation of errors when the measured Z_{dr} is close to 0 dB).

As mentioned earlier, the PPI scans for both events covered the six 2DVD sites (Figs. 1b,c). Bringi et al. (2013a) compared Z_h, Z_{dr}, and R determined from NPOL data with simultaneous measurements from all six 2DVDs. Very good agreement was found for all three quantities, and, furthermore, rain accumulations also showed good agreement. Further information can be found in Bringi et al. (2013a) and Thurai et al. (2012). Furthermore, in Bringi et al. (2013b), D_0 comparisons between NPOL data–based estimation using Eq. (3) above and the 2DVD-based estimation have been made. For the latter, 1-min DSDs were used for fitting to the normalized gamma distribution as in Bringi et al. (2003). Excellent agreement was found between the two time series comparisons for all six 2DVD locations and for both events. For the 24 April 2011 event, which was a much more rapidly evolving storm, D_0 values were seen to vary rapidly, for example, from 3 mm to less than 1 mm within 30 min for one of the 2DVD locations, but even so, the agreement between the NPOL-derived D_0 and the 2DVD-measured D_0 was found to be very good, except perhaps at the beginning of the storm, where drop sorting may have played a role. The relative frequency histograms of radar-derived and disdrometer-calculated D_0 were constructed for both events (not shown here) and were found to be in excellent agreement in terms of mean, standard deviation, and skewness.

b. *Horizontal correlations from PPI scans*

To calculate the correlation coefficients (Pearson product moment correlation estimator) for each variable [D_0, $\log_{10}(N_W)$, and R] defining the vector $\mathbf{v}$ from the PPI scans, a three-dimensional volume V is defined with dimensions $G \times B \times T$ (see Fig. 3a), where G is the total number of gates in the radial direction, B is the total number of beams in a single PPI scan, and T is the total number of scans in the time interval of interest (0929–1042 UTC 24 April and 1909–2333 UTC 11 May). Note that the beam spacing is approximately 0.5° (azimuth angle span from 245° to 325° and thus B = 160). The Pearson correlation coefficient computed from radar data is necessarily pixel or areal based as opposed to point correlations from gauges. Whereas Moreau et al. (2009)

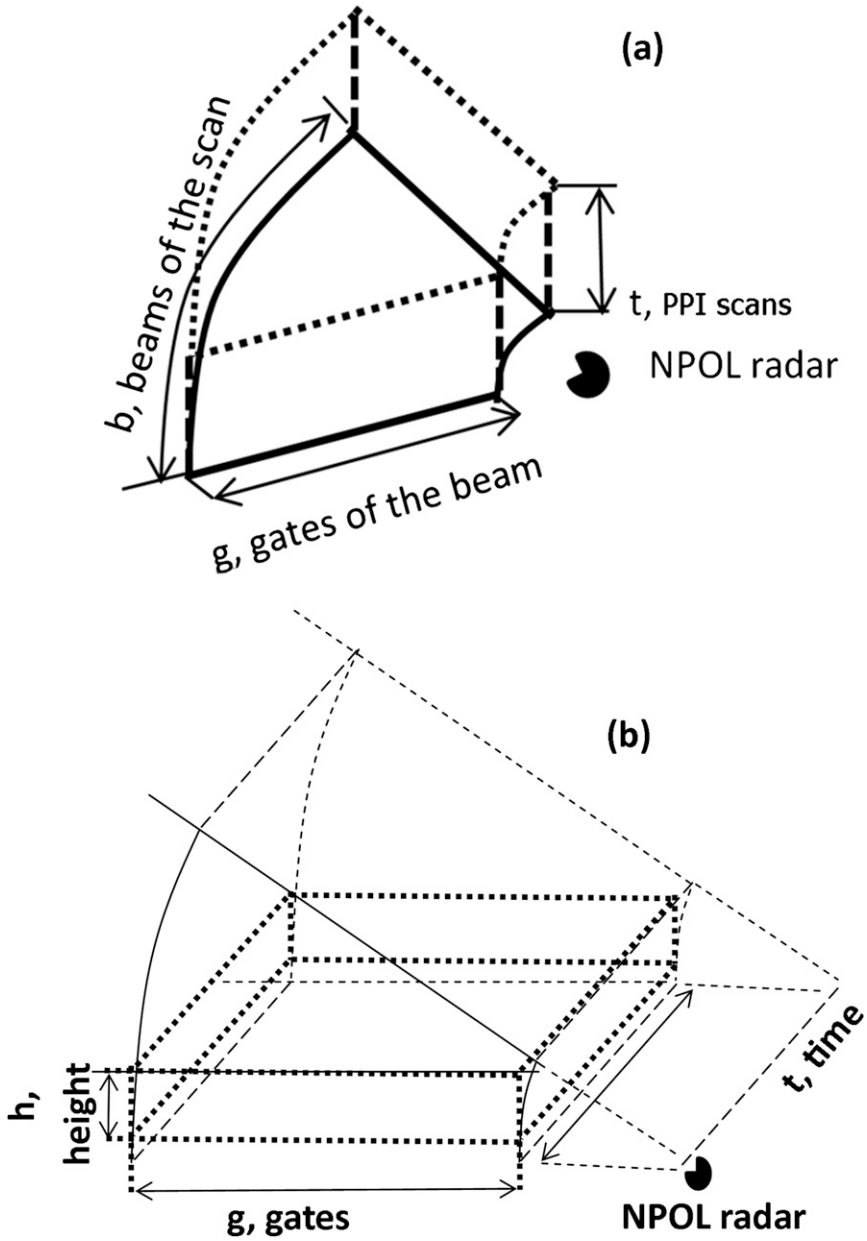

FIG. 3. (a) The 3D volume, created for each radar variable in the vector **v**, shown relative to the location of NPOL. The initial start range is 20 km for 24 Apr and 25 km for 11 May. (b) The 3D volume (dotted line) after interpolation from cylindrical (radar) coordinates into Cartesian coordinates and limiting lower altitude to 0.6 km and upper altitude to 3 km, created for each radar variable in the vector **v**.

transform their radar-based areal ($1 \times 1\,\mathrm{km}^2$) correlations to point correlations, the polar pixels defined here are much smaller (typically, $200 \times 150\,\mathrm{m}^2$ at 25-km range), and hence, we do not distinguish between areal and point correlations. Considering the argument that the logarithmic transformation of R should be used to avoid bias in the correlation coefficient (because of strong positive skewness of the PDF of R), the bias is small (<0.07 or so; Habib and Krajewski 2002) for short time scales ($\sim$5 min), and thus we follow CK06, who did not use the logarithmic transformation of R in their extensive study of spatial correlations from a large database of Oklahoma storms. The PDF of D_0 is generally quite symmetric without significant skewness (e.g., Bringi et al. 2003, 2012; Thurai and Bringi 2008), so no logarithmic transformation is necessary. In the case of N_W, in

addition to its large range of values spanning several orders of magnitude (Illingworth and Blackman 2002; Bringi et al. 2003), the distribution can be significantly positively skewed (Bringi et al. 2003), so the logarithmic transformation is used as such.

The resulting matrix of Pearson's correlation coefficient $\mathbf{C}$ has dimensions $G \times B$, and each element of this matrix is calculated using the MATLAB function corr(), which compares two 1D arrays of data, each one being the time sequence [meaning it includes interpolated data at the specific position (g, b) of all PPI scans $1, \ldots, T$ of the time interval of interest]:

$$\mathbf{C}_{gb} = \mathrm{corr}(v_{1b1,\ldots,T}, v_{gb1,\ldots,T}), \tag{9}$$

where g $(1, \ldots, G)$ is the number of the gate from the starting point, and b $(1, \ldots, B)$ is the number of the beam. Here the "base" time sequence for each beam is the closest to the radar in the range of interest and is sequentially compared to those farther from the radar, thereby creating a column of correlation coefficient values in matrix $\mathbf{C}$. Only those gates that are not "NaN," or not a number, indicating no data or no meteorological echo, in both base and next-in-range time sequences are used in the correlation calculations.

To reduce high-frequency data fluctuations along the time axis (recall PPI scans were repeated every 40 s), the time sequences are smoothed using a weighted moving average filter with window size 9, which corresponds to effective averaging time scale of approximately 2.5 min. The effect of temporal averaging on the spatial correlation function from gauge data has been well described by CK06.

c. *Vertical correlations from RHI scans*

Vertical correlation coefficients are calculated from the RHI scans in a similar manner. The three variables, D_0, $\log_{10}(N_W)$, and LWC, defining the vector $\mathbf{v}$, are interpolated from radar coordinates (elevation, range) to a (x, z) Cartesian grid. We use LWC as opposed to R for vertical correlations since the radar-based retrieval is for still air rain rates and not applicable in the presence of vertical air motion. The beam spacing is around 0.2°, and at a range of 30 km, the vertical separation is close to 100 m. The dimensions of each cell of the grid were chosen to be $150 \times 100\,\mathrm{m}^2$, so that the horizontal spacing (along x coordinate) corresponds to that of the original radar range gate spacing. The RHI scans were repeated every 40 s at fixed azimuth angle (see Fig. 3b, which shows the time axis and the volume). The selected data begin at a height (z coordinate) of 0.6 km from the ground (to avoid problems due to ground clutter) and end around 0.5 km below the brightband height (at ~3 km, see Fig. 2). Further, data from the 15–38 km range interval are selected for 24 April and 20–36 km for 11 May; these range limits provide for continuous time series of "good" data at each pixel necessary for the correlation estimation. Then, for each variable in the vector $\mathbf{v}$, the 3D volume is defined. Each volume has dimensions $P \times H \times T$, where P is the total number of cells in the radial (after gridding referred to as the horizontal) direction, H is the total number of cells of the interpolation grid in vertical direction, and T is the total number of RHI scans made by radar in the time interval of interest (0929–1042 UTC 24 April and 1909–2333 UTC 11 May).

The resulting matrix of Pearson's correlation coefficients $\mathbf{C}$ has dimensions $P \times H$, and each element of this matrix is calculated using MATLAB function corr(), which compares two 1D arrays of data, each one being a time sequence [meaning it includes data at specific position (g, h) of all RHI scans $1, \ldots, T$ of the time interval of interest]:

$$\mathbf{C}_{gh} = \mathrm{corr}(v_{g11,\ldots,T}, v_{gh1,\ldots,T}), \tag{10}$$

where g is a cell number in the horizontal direction, starting from the beginning mark (15 km for 24 April and 20 km for 11 May), and h is a cell number in vertical direction, starting from the lowest height mark (0.6 km base or reference height, where by definition the correlation coefficient is 1). At each horizontal position, the lowest (base) time sequence $v_{g11,\ldots,T}$ is sequentially compared to each time sequence $v_{gh1,\ldots,T}$ above it, to get a column of correlation coefficients in the matrix $\mathbf{C}$.

Again, to reduce high-frequency data fluctuations along the time axis (recall RHI scans were repeated every 40 s), the time sequences are smoothed using a weighted moving average filter with window size 9, which corresponds to effective averaging time scale of approximately 2.5 min.

4. Results

a. *Spatial correlation: Convective and stratiform rain examples*

The results presented here are a generalization of Thurai et al. (2012), who used radar data in a 1D perspective (i.e., radar beam essentially dwelling over two 2DVDs located at a range of 15 km) transformed to a 2D perspective where the radar beam scans over a 80° azimuth sector (within which six 2DVD units are located) with a revisit time of 40 s.

The horizontal correlation coefficients computed for D_0 using the aforementioned procedures (see section 3b) are represented as a 2D map of correlation coefficients in Figs. 4a and 4b for the 24 April and the 11 May 2011

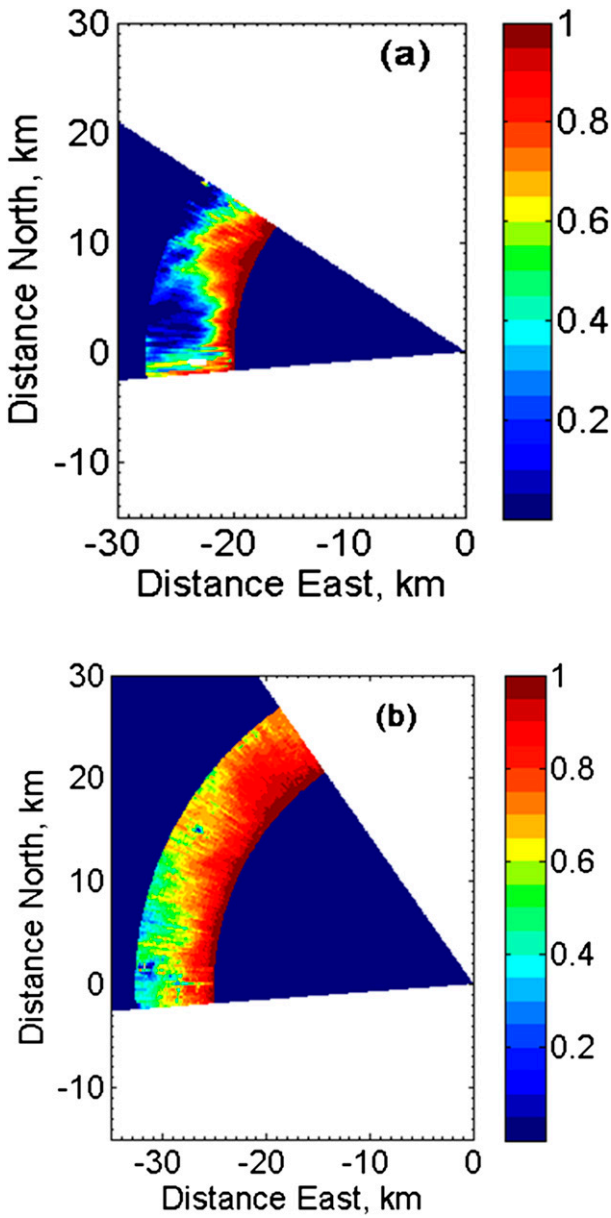

FIG. 4. PPI maps of correlation coefficient for D_0 for (a) 24 Apr (convective) and (b) 11 May (stratiform). Note reference range where correlation is 1 is 20 km in (a) and 25 km in (b).

events, respectively. The initial (henceforth reference) range and azimuth sector for 24 April are selected as 20 km and (265°–305°), respectively, whereas for 11 May the corresponding values are 25 km and (265°–345°). These selections are based on visual inspection of the spatiotemporal evolution of the two precipitation events to ensure that time sequences of good data (i.e., meteorological echo) are available for all polar pixels. By definition then, nonraining pixels as determined by the radar sensitivity and detection of nonmeteorological echo are excluded. For the highly convective 24 April event, strong azimuthal dependence and faster falloff with distance can be noted relative to the more uniform 11 May event. Note that the correlation coefficient is 1 by definition at the reference range. Moving this reference range radially did not change the azimuthal variability or the falloff with distance. While the azimuthal dependence and correlation falloff appear reasonable considering the differences (convective versus stratiform) between the two events, there are, to the best of our knowledge, no other radar-based calculations in the literature with which we can compare. However, gauge networks have been used to determine 2D maps of correlation coefficients of 1-min R for various rainfall types, one early example being Huff (1970).

To construct pseudo-1D correlation coefficient versus distance functions that can be compared with other radar or gauge-based data, we proceed as follows. From the set of correlation coefficients at a fixed range through the angular sector, we construct the cumulative distribution function (CDF) of the spatial correlation and compute the 10th, 50th (median), and 90th percentile values. This is repeated at range increments of 150 m (radar gate spacing). Such an approach gives a pseudo-1D spatial correlation versus distance while at the same time giving an estimate of its cross-beam (azimuthal) variability. Figures 5a–c show the pseudo-1D spatial correlation for the three variables, D_0, $\log_{10}(N_W)$, and R, respectively, for the 24 April event, and Figs. 5d–f show the corresponding figures for the 11 May event. In all cases, the curves corresponding to the 10th, 50th, and 90th percentiles are shown. Some general points can be made from examination of Fig. 5. First, the median correlation falls off faster with increasing distance for the 24 April event compared with the 11 May event. Second, the azimuthal variability as measured by the spread between the 10th and 90th percentile values is much larger for 24 April versus 11 May. However, in absolute terms, the spread for the 24 April event is quite large, especially for distances >1.5 km. For R the spread seems consistent with the $\pm 2\sigma$ uncertainty bounds provided by Habib and Krajewski (2002; their Fig. 7) and Gebremichael and Krajewski (2004; their Fig. 2).

Krajewski et al. (2003) have used a three-parameter modified-exponential function of the form

$$\rho(d) = \rho_0 \exp[-(d/R_0)^F]. \tag{11}$$

Here d is the distance, R_0 is the decorrelation distance (1/e-folding distance), F is a shape parameter, and ρ_0 is the correlation when $d = 0$ (i.e., the "nugget" parameter). Tables 2 and 3 compare the R_0 and F parameters fitted to the pseudo-1D median correlation versus distance data shown in Fig. 5 (the "nugget" parameter is 1

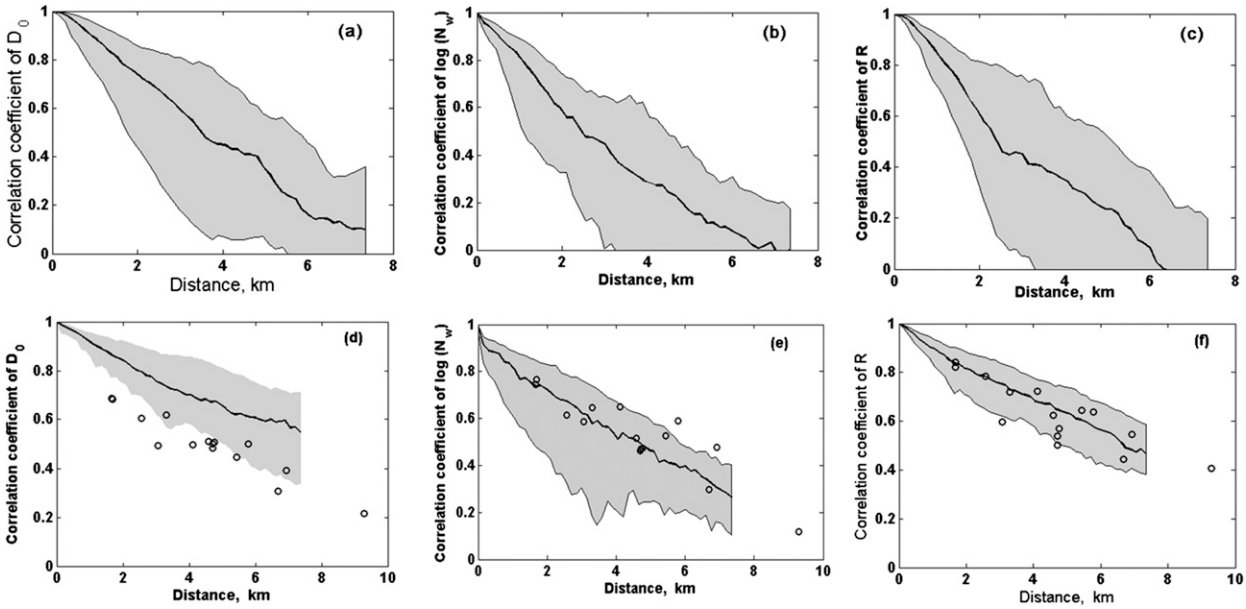

FIG. 5. Psuedo-1D spatial correlation coefficient of (a) D_0, (b) $\log_{10}(N_W)$, and (c) R for the 24 Apr convective event. Solid line is the median curve and lower (upper) bounds are the 10th (90th) percentile. Distance is from reference range of 20 km. (d)–(f) As in (a)–(c), but for the stratiform 11 May event. Distance is relative to reference range of 25 km. Open circles are spatial correlation values from the 2DVD network.

for the radar-based calculations). The decorrelation distance is consistently smaller for all variables for 24 April as compared with 11 May. On the other hand, the shape factor is consistently >1.4 for 24 April (convex down as one approaches $d = 0$), whereas for 11 May it is close to 1 (exponential falloff). Such variability in F is consistent with the spread of values reported by CK06 for 3-min R correlation fits for a large database of Oklahoma storms. For storms they classified as low and high variability, they found the fit parameters for 3-min R as (9.8 km, 1.47) and (4.4 km, 1.24), respectively, but they also found large storm-to-storm variations (their Fig. 9). In comparison, Tables 2 and 3 show (10.2 km, 1.0) and (3.4 km, 1.52), that is, good agreement comparing gauge- versus radar-derived fit parameters.

Thurai et al. (2012) obtained (R_0, F) values for D_0, $\log_{10}(N_W)$, and R as (8.24 km, 1.36), (7.22 km, 1), and (4.74 km, 1.28), respectively, for a widespread stratiform rain event with embedded convection. Their 1D radar-based correlation fits (similar pixels and time resolutions) are in reasonable agreement with fits to the median correlation data for the 11 May event. Moreau et al. (2009) obtained (4.54 km, 1.3) as their fit to radar-based correlation of R at 6-min resolution and $1 \times 1\,\mathrm{km}^2$ pixels using a 1-yr database, which compares reasonably well with our 24 April event (3.4 km, 1.52).

For the long-duration 11 May event, the 2DVD network is used to compute the spatial correlation of [D_0, $\log_{10}(N_W)$, and R], the distances ranging from 1.5 to 7 km (open circles in Figs. 5d–f). The 1-min time series of DSDs were fitted to a normalized gamma distribution as in Bringi et al. (2003). Further, the time series were smoothed with the same weighted moving average filter as used for the radar time series. As seen in Figs. 5e and 5f, the 2DVD-based spatial correlations fall remarkably well within the 10th and 90th percentile radar-based values both for $\log_{10}(N_W)$ and R; however, for D_0 they fall closer to the 10th percentile and offset downward from the radar-based median curve by around 0.15. The reason for this behavior is not readily apparent. One possibility is that the radar-based retrieval of D_0 could be biased (i.e., systematic errors) as the retrieval algorithm in Eq. (3) is based on disdrometer (point) measurements and then applied to a much larger radar sample volume. However, as discussed in the last paragraph of section 2a, the relative frequency histograms of radar-derived and disdrometer-calculated D_0 for the two events showed excellent agreement with respect to mean, standard deviation, and skewness. Thus, it is

TABLE 2. Fitting coefficients (R_0, F) for variables D_0, $\log_{10}(N_W)$, and R for the median horizontal correlation for the convective case (24 Apr).

24 Apr 2011	R_0 (km)	F
D_0	4.5	1.57
R	3.4	1.52
$\mathrm{Log}_{10}(N_W)$	3.25	1.4

TABLE 3. Fitting coefficients (R_0, F) for variables D_0, $\log_{10}(N_W)$, and R for the median horizontal correlation for the stratiform case (11 May).

11 May 2011	R_0 (km)	F	R_0*	F*
D_0	12.8	0.91	8.9	0.64
R	10.2	1.0	7.5	0.6
$\text{Log}_{10}(N_W)$	6.35	0.93	2.74	0.50

* These fitted coefficients are for time window averaging of length = 3.

unlikely that the radar-derived D_0 spatial variability is being artificially reduced by retrieval bias errors. If this were true, it should also apply to $\log_{10}(N_W)$ and R, which is clearly not the case. Moreover, the general agreement depicted in Fig. 5 gives confidence in the radar-derived spatial correlations for the 11 May event and, by inference, for the 24 April event as well. Note that the latter was of much shorter duration (70 min versus 4 h for 11 May) and highly convective, which precluded stable estimates of the spatial correlation from the 2DVD network configuration. To test if the hypothesis of better agreement between the radar- and 2DVD-derived spatial correlations for D_0 could be achieved by using a shorter-sized window filter for the radar time series, Fig. 6 shows the result for window length of 3 corresponding to an averaging time scale of approximately 60 s (recall that in Fig. 5 the window length is 9 corresponding to an averaging time scale of approximately 2.5 min). The results of Fig. 6, which in essence decrease the radar-based spatial correlation values (i.e., more variability) with decreasing time resolution, thereby nicely encompassing the 2DVD-based values within the 10th and 90th percentiles, agree with the well-known effect demonstrated by many studies using gauge networks that spatial correlation, in general, decreases with decrease in the time averaging (e.g., CK06). See Table 3, where the fitted values of R_0 and F are given for the shorter-sized window length of 3.

b. *Spatial correlations along vertical: Convective and stratiform examples*

To determine vertical correlations, we use the repeated RHI scans, which were made along an azimuth of 283.5° as part of the scan sequence (see section 2c). For each variable we compute and plot a map of correlation coefficients, which demonstrates the decrease of correlation coefficient as a function of height for each range. In all cases, the reference height was set to be 0.6 km in order to avoid problems due to ground clutter. Furthermore, as mentioned earlier, the brightband height for the 11 May event was around 3 km (see Fig. 2d), whereas for the highly convective 24 April case the melting level

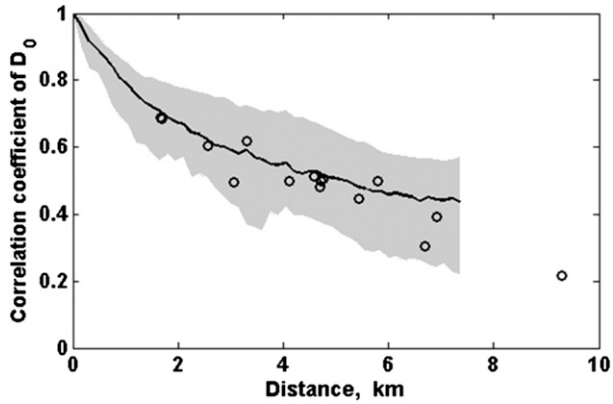

FIG. 6. As in Fig. 5d, but for radar time series filtered using a weighted moving average window of length 3.

varied somewhat because of updrafts/downdrafts; still, Fig. 2d shows a bright band at 1100:00 UTC at a height of 2.7 km. To be consistent, the correlation coefficients for both events were calculated for heights up to 2.4 km above the reference height of 0.6 km (where the correlation coefficient, by definition, is 1).

Figures 7a and 7b show D_0 for the two events. The decrease in the correlation coefficients with height is evident in both cases, but for the 24 April case, the decrease is considerably faster (more vertical variability) compared with the stratiform rain event on 11 May. The rapid falloff above 2 km, especially for the 24 April case, indicates decorrelation due to the melting layer. It is not possible to quantitatively assess decorrelation due to the melting layer or the bright band versus that due to rain DSD variability near the 2–2.5-km height in these two events. In Fig. 7a, there are isolated pixels where the spatial correlation is obviously incorrect. This is due to the time series of data from these pixels being identified as nonmeteorological echoes by our classification algorithm (subset of the entire time series at the given pixel classified as nonmeteorological, which when correlated with fully meteorological time series from the reference pixel, leads to isolated errors in the spatial correlation calculation).

Analogous to the derivation of horizontal correlations from the PPI scans, the set of correlation coefficients at a fixed height (starting reference height at 0.6 km) and along the radial direction are used to construct the appropriate CDF of the spatial correlations from which the 10th, 50th (median), and 90th percentile values are obtained. This is repeated at height increments of 100 m. This yields the pseudo-1D height correlation at the same time, giving an estimate of along-range variability.

Figures 8a and 8b show the pseudo-1D height correlation of D_0 for the two events, once again as 10th, 50th, and 90th percentile curves. Note that the correlation falls

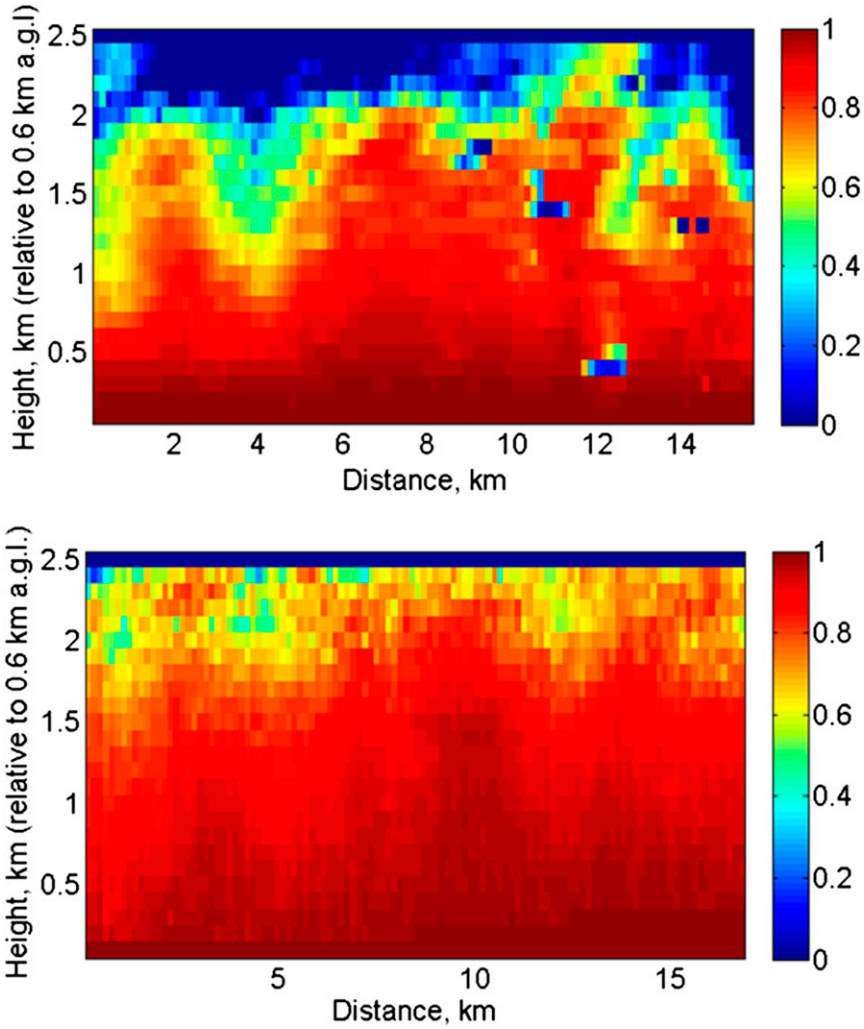

FIG. 7. RHI maps of the D_0 correlation coefficients for (a) 24 Apr (convective case) and (b) 11 May (stratiform case). The y axis is height relative to 0.6 km. For 24 Apr the radial reference distance is 15 km (and extends to 31 km) whereas for 11 May the radial reference distance is 20 km (and extends to 38 km).

off significantly faster for the 24 April convective rain compared to the stratiform 11 May event, perhaps not unexpectedly. The corresponding curves for $\log_{10}(N_W)$ are shown in Figs. 8c and 8d. The spread between the 10th and 90th percentile curves is much larger for 24 April as compared to 11 May, similarly to the horizontal correlations but not as pronounced. Such vertical correlation data for DSD parameters are expected to be useful, for example, for both ground radar as well as satellite-based radars, where retrievals are made aloft (~1.5 km AGL) but need to be extrapolated down to the surface. Finally, Tables 4 and 5 give the fit parameters (R_0, F) using the median vertical correlation data [Eq. (11)] for the two events. While the values appear reasonable, there are no equivalent data to compare with as yet in the literature, but profilers (dual wavelength) that retrieve the DSD parameters could easily be used to validate the results shown herein (Williams and Gage 2009), at least for the stratiform rain case. Some caution should be exercised in using the fit parameters in Tables 4 and 5 for the convective event since the stationarity assumption may not be valid, for example, because of vertical air motion.

5. Summary and conclusions

Two events during the MC3E campaign are analyzed using NPOL data and a network of six closely spaced 2DVD instruments. One event (24 April 2011) was strongly convective and was of much shorter duration

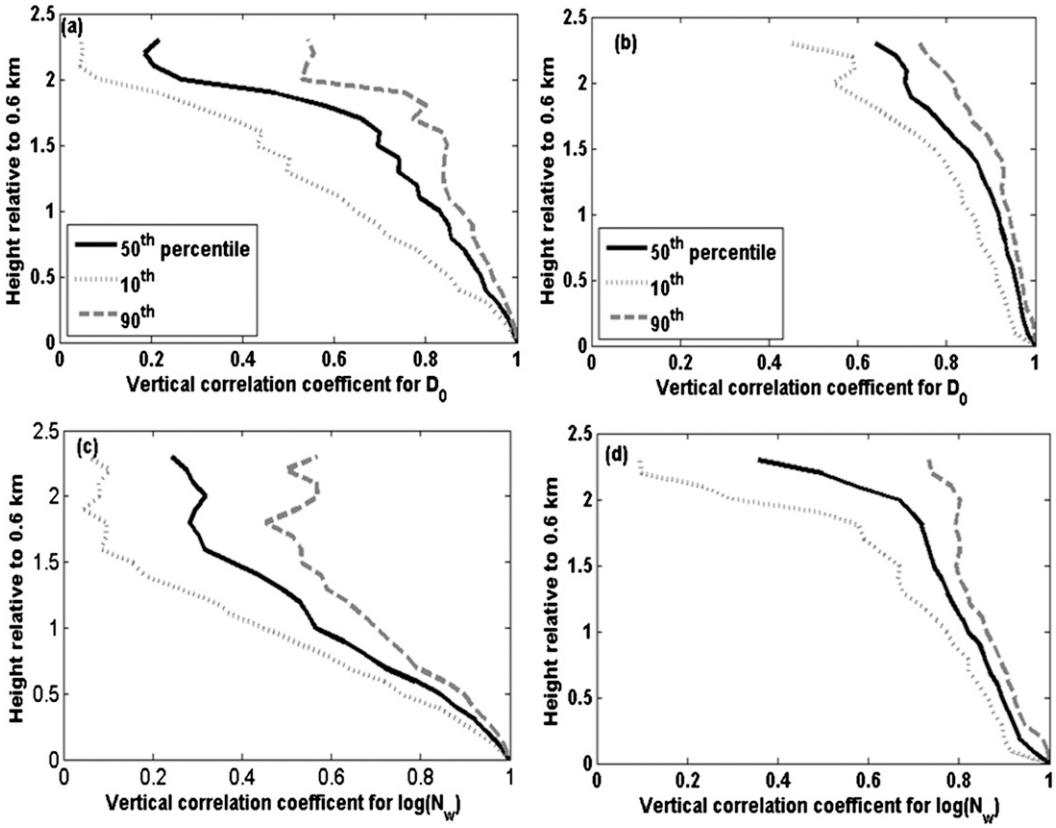

FIG. 8. Comparing D_0 percentiles for (a) 24 Apr (convective case) and (b) 11 May (stratiform case). (c),(d) As in (a),(b), but for $\log_{10}(N_W)$.

(<75 min) over the 2DVD network, and the second event (11 May 2011) was of longer duration (around 4 h) and much more widespread, with large areas of stratiform rain.

Retrieval algorithms for D_0, N_W, and R were derived using the 2DVD data and applied to NPOL measurements. From the repeated PPI scans, with 40-s revisit time, we derive the spatial (horizontal) correlations for the two events at an averaging time scale of approximately 2.5 min and radar pixels of size around $150 \times 250\,\mathrm{m}^2$. The azimuthal dependence of the spatial correlation of D_0 showed considerable variation for the convective event as compared with the stratiform event. A pseudo-1D spatial correlation versus distance was derived for D_0, $\log_{10}(N_W)$, and R for the two events and fitted to a modified-exponential function with parameters being the decorrelation distance (1/e-folding distance) (R_0) and the shape factor (F). The convective event showed considerable spatial variability, with lower values of R_0 relative to the stratiform event. The fit parameters for R were found to be generally consistent with other studies mainly based on gauges/disdrometers at similar spatial and temporal scales. For the long-duration stratiform event, the 2DVD network was used to calculate the spatial correlation of D_0, $\log_{10}(N_W)$, and R and compared with the pseudo-1D radar-derived correlations. The $\log_{10}(N_W)$ and R correlations from radar agreed very well with the 2DVD-based correlations,

TABLE 4. Fitting coefficients (R_0, F) for variables D_0, $\log_{10}(N_W)$, and LWC for the median vertical correlation for the convective case (24 April).

24 Apr 2011	R_0 (km)	F
D_0	2.65	1.68
$\mathrm{Log}_{10}(N_W)$	1.55	1.46
LWC	2.60	1.25

TABLE 5. Fitting coefficients (R_0, F) for variables D_0, $\log_{10}(N_W)$, and LWC for the median vertical correlation for the stratiform case (11 May).

11 May 2011	R_0 (km)	F
D_0	3.77	1.80
$\mathrm{Log}_{10}(N_W)$	6.44	0.86
LWC	3.03	2.0

but rather surprisingly, the D_0 correlations from 2DVD fell off faster than from radar. Adjusting the time averaging of the radar D_0 estimates brought the radar and 2DVD-based correlations into better agreement, which is expected given the well-known property that spatial correlations decrease (more variability) with decreasing time averaging.

Vertical correlations are also calculated from repeated RHI scans with 40-s revisit times. The radar retrievals were interpolated to a Cartesian grid with spacing $150 \times 200\,\mathrm{m}^2$. Similar to the horizontal correlations, the convective event showed significantly more variability along the vertical as compared with the stratiform event. A pseudo-1D spatial correlation versus height was generated and fitted to the modified-exponential function, which clearly showed the convective versus stratiform differences based on the decorrelation distance. Some caution should be exercised in interpreting the fit parameters for the convective case because of nonstationarity, for example, due to vertical air motions. The vertical correlations, while believed to exhibit reasonable behavior, could not be validated but could be done so in the future using D_0 and N_W estimated from profilers.

With the caveat that only two events are analyzed, this study nevertheless shows that dual-polarimetric radar can be used to derive spatial correlations of DSD parameters and rain rate if the scan cycle (revisit) time is kept short (<1 min), and relative to gauge networks, a much smaller database is needed by virtue of the dense availability of radar pixels. The radar-derived spatial correlations and fits can thus be used in a variety of applications, for example, error variance separation in radar–gauge intercomparisons, downscaling methodologies, non-uniform beam filling corrections for satelliteborne radar retrievals which involve larger pixels ($5 \times 5\,\mathrm{km}^2$ for GPM Dual-Frequency Precipitation Radar), and range-dependent error characterizations. It even applies to coarse-scale radar estimates, for example, at long ranges where the radar beam becomes broad, or even grid-averaged products. In many of the above applications, the assumptions of isotropy (to some extent quantified herein) of the spatial correlation function as well as stationarity of the underlying process need to be invoked, which have yet to be addressed.

Acknowledgments. We thank the NPOL scientists and technicians as well as the disdrometer field technicians during MC3E for collecting the data used in this study. We would also like to thank Dr. R. Kakar of the NASA Precipitation Measurement Mission and Dr. A. Hou and Dr. M. Schwaller of the NASA GPM program offices for providing funding for this study. The S-band profiler data shown in Figs. 2b and 2d were provided by Dr. C. R. Williams.

REFERENCES

Aydin, K., T. A. Seliga, and V. Balaji, 1986: Remote sensing of hail with a dual linear polarization radar. *J. Appl. Meteor.,* **25,** 1475–1484, doi:10.1175/1520-0450(1986)025<1475:RSOHWA>2.0.CO;2.

Brandes, E. A., C. J. Kessinger, J. D. Tuttle, and J. Vivekanandan, 1993: An evaluation of multiparameter radar measurements for detecting hail. Preprints, *26th Conf. on Radar Meteorology,* Norman, OK, Amer. Meteor. Soc., 522–524.

Bringi, V. N., V. Chandrasekar, J. Hubbert, E. Gorgucci, W. L. Randeu, and M. Schoenhuber, 2003: Raindrop size distribution in different climatic regimes from disdrometer and dual-polarized radar analysis. *J. Atmos. Sci.,* **60,** 354–365, doi:10.1175/1520-0469(2003)060<0354:RSDIDC>2.0.CO;2.

——, M. Thurai, K. Nakagawa, G.-J. Huang, T. Kobayashi, A. Adachi, H. Hanado, and S. Sekizawa, 2006: Rainfall estimation from C-band polarimetric radar in Okinawa, Japan: Comparisons with 2D-video disdrometer and 400 MHz wind profiler. *J. Meteor. Soc. Japan,* **84,** 705–724, doi:10.2151/jmsj.84.705.

——, C. R. Williams, M. Thurai, and P. T. May, 2009: Using dual-polarized radar and dual-frequency profiler for DSD characterization: A case study from Darwin, Australia. *J. Atmos. Oceanic Technol.,* **26,** 2107–2122, doi:10.1175/2009JTECHA1258.1.

——, M. A. Rico-Ramirez, and M. Thurai, 2011: Rainfall estimation with an operational polarimetric C-band radar in the United Kingdom: Comparison with a gauge network and error analysis. *J. Hydrometeor.,* **12,** 935–954, doi:10.1175/JHM-D-10-05013.1.

——, G.-J. Huang, S. J. Munchak, C. D. Kummerow, D. A. Marks, and D. B. Wolff, 2012: Comparison of drop size distribution parameter (D_0) and rain rate from S-band dual-polarized ground radar, TRMM Precipitation Radar (PR), and combined PR–TMI: Two events from Kwajalein Atoll. *J. Atmos. Oceanic Technol.,* **29,** 1603–1616, doi:10.1175/JTECH-D-11-00153.1.

——, M. Thurai, W. A. Petersen, and P. N. Gatlin, 2013a: Using a network of 2D video disdrometers for external radar calibration of NASA's S-band polarimetric radar. *36th Conf. on Radar Meteorology,* Breckenridge, CO, Amer. Meteor. Soc., 10.3. [Available online at https://ams.confex.com/ams/36Radar/webprogram/Paper228161.html.]

——, L. Tolstoy, M. Thurai, and W. A. Petersen, 2013b: Estimation of spatial correlation of rain drop size distribution parameters and rain rates using NASA's S-band polarimetric radar and 2D video disdrometer network: Two case studies from MC3E. *36th Conf. on Radar Meteorology,* Breckenridge, CO, 240. [Available online at https://ams.confex.com/ams/36Radar/webprogram/Paper228159.html.]

Chandrasekar, V., V. N. Bringi, S. A. Rutledge, A. Hou, E. Smith, G. Skofronick Jackson, E. Gorgucci, and W. A. Petersen, 2008: Potential role of dual-polarization radar in the validation of satellite precipitation measurements: Rationale and opportunities. *Bull. Amer. Meteor. Soc.,* **89,** 1127–1145, doi:10.1175/2008BAMS2177.1.

Ciach, G. J., and W. F. Krajewski, 2006: Analysis and modeling of spatial correlation structure of small-scale rainfall in central Oklahoma. *Adv. Water Resour.,* **29,** 1450–1463, doi:10.1016/j.advwatres.2005.11.003.

Depue, T., P. Kennedy, and S. Rutledge, 2007: Performance of the hail differential reflectivity (HDR) polarimetric hail indicator. *J. Appl. Meteor. Climatol.,* **46,** 1290–1301, doi:10.1175/JAM2529.1.

Gebremichael, M., and W. F. Krajewski, 2004: Assessment of the statistical characterization of small-scale rainfall variability from radar: Analysis of TRMM ground validation datasets. *J. Appl. Meteor.,* **43,** 1180–1199, doi:10.1175/1520-0450(2004)043<1180:AOTSCO>2.0.CO;2.

Habib, E., and W. F. Krajewski, 2002: Uncertainty analysis of the TRMM ground-validation radar–rainfall products: Application to the TEFLUN-B field campaign. *J. Appl. Meteor.,* **41,** 558–572, doi:10.1175/1520-0450(2002)041<0558:UAOTTG>2.0.CO;2.

Hou, A. Y., and Coauthors, 2014: The Global Precipitation Measurement Mission. *Bull. Amer. Meteor. Soc.,* **95,** 701–722, doi:10.1175/BAMS-D-13-00164.1.

Huang, G-J., V. N. Bringi, and M. Thurai, 2008: Orientation angle distributions of drops after an 80-m fall using a 2D video disdrometer. *J. Atmos. Oceanic Technol.,* **25,** 1717–1723, doi:10.1175/2008JTECHA1075.1.

Hubbert, J., and V. N. Bringi, 1995: An iterative filtering technique for the analysis of copolar differential phase and dual-frequency radar measurements. *J. Atmos. Oceanic Technol.,* **12,** 643–648, doi:10.1175/1520-0426(1995)012<0643:AIFTFT>2.0.CO;2.

Huff, F. A., 1970: Spatial and temporal correlation of precipitation in Illinois. ISWS/CIR-141/79, Illinois Institute of Natural Resources, 14 pp.

Illingworth, A. J., and T. M. Blackman, 2002: The need to represent raindrop size spectra as normalized gamma distributions for the interpretation of polarimetric radar observations. *J. Appl. Meteor.,* **41,** 286–297, doi:10.1175/1520-0450(2002)041<0286:TNTRRS>2.0.CO;2.

Jaffrain, J., and A. Berne, 2012: Influence of the subgrid variability of the raindrop size distribution on radar rainfall estimators. *J. Appl. Meteor. Climatol.,* **51,** 780–785, doi:10.1175/JAMC-D-11-0185.1.

Kozu, T., and T. Iguchi, 1999: Nonuniform beamfilling correction for spaceborne radar rainfall measurement: Implications from TOGA COARE radar data analysis. *J. Atmos. Oceanic Technol.,* **16,** 1722–1735, doi:10.1175/1520-0426(1999)016<1722:NBCFSR>2.0.CO;2.

Krajewski, W. F., G. J. Ciach, and E. Habib, 2003: An analysis of small-scale rainfall variability in different climatic regimes. *Hydrol. Sci.,* **48,** 151–162, doi:10.1623/hysj.48.2.151.44694.

Lee, C. K., G. W. Lee, I. Zawadzki, and K.-E. Kim, 2009: A preliminary analysis of spatial variability of raindrop size distributions during stratiform rain events. *J. Appl. Meteor. Climatol.,* **48,** 270–283, doi:10.1175/2008JAMC1877.1.

Löffler-Mang, M., and J. Joss, 2000: An optical disdrometer for measuring size and velocity of hydrometeors. *J. Atmos. Oceanic Technol.,* **17,** 130–139, doi:10.1175/1520-0426(2000)017<0130:AODFMS>2.0.CO;2.

Meneghini, R., H. Kim, L. Liao, and J. Jones, 2013: Dual-frequency spaceborne retrieval methods and the role of non-uniform beam filling. *36th Conf. on Radar Meteorology,* Breckenridge, CO, Amer. Meteor. Soc., 9A.4. [Available online at https://ams.confex.com/ams/36Radar/webprogram/Paper228626.html.]

Moore, R. J., D. A. Jones, D. R. Cox, and V. S. Isham, 2000: Design of the HYREX raingauge network. *Hydrol. Earth Syst. Sci.,* **4,** 521–530, doi:10.5194/hess-4-521-2000.

Moreau, E., J. Testud, and E. Le Bouar, 2009: Rainfall spatial variability observed by X-band weather radar and its implication for the accuracy of rainfall estimates. *Adv. Water Resour.,* **32,** 1011–1019, doi:10.1016/j.advwatres.2008.11.007.

Petersen, W., and M. Jensen, 2012: The NASA-GPM and DOE-ARM Midlatitude Continental Convective Clouds Experiment (MC3E). *The Earth Observer,* Vol. 24, Issue 1, Earth Observing System Project Science Office, NASA GSFC, Greenbelt, MD, 12–18. [Available online at http://eospso.gsfc.nasa.gov/sites/default/files/eo_pdfs/Jan_Feb_2012_col_508.pdf.]

Ryzhkov, A. V., S. E. Giangrande, and T. J. Schuur, 2005: Rainfall estimation with a polarimetric prototype of WSR-88D. *J. Appl. Meteor.,* **44,** 502–515, doi:10.1175/JAM2213.1.

Schleiss, M., and A. Berne, 2012: Stochastic space–time disaggregation of rainfall into DSD fields. *J. Hydrometeor.,* **13,** 1954–1969, doi:10.1175/JHM-D-12-013.1.

Schönhuber, M., G. Lammer, and W. L. Randeu, 2008: The 2D-video-distrometer. *Precipitation: Advances in Measurement, Estimation and Prediction,* S. Michaelides, Ed., Springer, 3–31, doi:10.1007/978-3-540-77655-0_1.

Short, D. A., and T. Iguchi, 2011: Model simulations of non-uniform beam filling correction for spaceborne precipitation radar. Preprints, *2011 IEEE Int. Geoscience and Remote Sensing Symp.,* Vancouver, BC, Canada, IEEE, 2594–2597, doi:10.1109/IGARSS.2011.6049772.

Tapiador, F. J., R. Checa, and M. de Castro, 2010: An experiment to measure the spatial variability of rain drop size distribution using sixteen laser disdrometers. *Geophys. Res. Lett.,* **37,** L16803, doi:10.1029/2010GL044120.

Thurai, M., and V. N. Bringi, 2008: Rain microstructure from polarimetric radar and advanced disdrometers. *Precipitation: Advances in Measurement, Estimation and Prediction,* S. Michaelides, Ed., Springer, 233–284, doi:10.1007/978-3-540-77655-0_10.

——, G.-J. Huang, V. N. Bringi, W. L. Randeu, and M. Schönhuber, 2007: Drop shapes, model comparisons, and calculations of polarimetric radar parameters in rain. *J. Atmos. Oceanic Technol.,* **24,** 1019–1032, doi:10.1175/JTECH2051.1.

——, V. N. Bringi, L. D. Carey, P. Gatlin, E. Schultz, and W. A. Petersen, 2012: Estimating the accuracy of polarimetric radar–based retrievals of drop-size distribution parameters and rain rate: An application of error variance separation using radar-derived spatial correlations. *J. Hydrometeor.,* **13,** 1066–1079, doi:10.1175/JHM-D-11-070.1.

Tokay, A., and P. G. Bashor, 2010: An experimental study of small-scale variability of raindrop size distribution. *J. Appl. Meteor. Climatol.,* **49,** 2348–2365, doi:10.1175/2010JAMC2269.1.

Villarini, G., P. V. Mandapaka, W. F. Krajewski, and R. J. Moore, 2008: Rainfall and sampling uncertainties: A rain gauge perspective. *J. Geophys. Res.,* **113,** D11102, doi:10.1029/2007JD009214.

Williams, C. R., and K. S. Gage, 2009: Raindrop size distribution variability estimated using ensemble statistics. *Ann. Geophys.,* **27,** 555–567, doi:10.5194/angeo-27-555-2009.